Wide-Band Polarization Control of Leaky Waves on Anisotropic Holograms

Amrollah Amini,[*] Homayoon Oraizi [,†] Mahsa Hamedani,[‡] and Ali Keivaan[§]

School of Electrical Engineering, Iran University of Science and Technology, 1684613114 Tehran, Iran

Isotropic leaky-wave holograms have great potential in the synthesis of single-beam and multibeam radiations in the desired directions. However, conventional methods are based only on the phase synthesis of the object wave front and do not have the ability to control the polarization of waves. A solution to this problem is the use of anisotropic holograms that provide more degrees of freedom. In this paper, the aperture field estimation theory is proposed for the synthesis of anisotropic holograms. Its advantage is the accurate prediction of far-field wave front characteristics, including phase, amplitude, and polarization. This method is used in the design of two different types of holograms in order to generate the pencil beam and vortex beam radiations. The pencil beam hologram is designed to have a high polarization purity across the visible region. In addition, a surface-wave reflector is implemented for eliminating the unwanted backward modes and adding a scannability property from 16 to 19 GHz to the hologram with an appropriate level of cross-polarization across the bandwidth. In the second section, the theoretical equations for the synthesis of vortex beam hologram with circular polarization is developed. As an example, an anisotropic hologram with topological charge of $l = 2$ is synthesized. Both theoretical and numerical results show that the anisotropic leaky-wave holograms are capable of generating orbital angular momentum (OAM) mode with the desired topological charge and polarization, which are simpler and more compact than other methods of generating OAM mode. For the proof of concept, a pencil beam hologram with a surface-wave reflector is fabricated and measured.

I. INTRODUCTION

The advent of two-dimensional (2D) and three-dimensional (3D) metamaterials has opened up new horizons for the manipulation of polarization, momentum, and other properties of electromagnetic waves. Recently, metasurfaces, as the 2D versions of metamaterials, have attracted attention in the electromagnetic engineering community. These structures provide many degrees of freedom in controlling the electromagnetic wave front by making abrupt phase shifts on the incident wave caused by the momentum change of the waves [1,2]. The change of wave front direction [3–5], polarization conversion [6–8], incident beam focusing [9,10], and cloaking [11] are attractive applications of metasurfaces. Some metasurfaces, often known as impedance surfaces, are also used in controlling surface waves. One common application of impedance surfaces is directing the electromagnetic waves in desired directions, such as surface-wave waveguides [12–15]. By making perturbations on these waveguides, metasurface leaky-wave structures are realized, which

have been popular in recent years. Leaky-wave structures can be used in a wide spectrum of applications, from microwaves to optical wavelengths [16–19]. Controlling the amount of leakage power, wave front direction, frequency scannability, and polarization conversion are of special importance in the design of leaky-wave antennas. One attractive approach for the synthesis of leaky-wave structures based on impedance surfaces is the use of holography theory in the microwave regime, initially introduced by Checcacci *et al.* [20]. In the theory of holography, the information obtained from the interference of reference and object waves is used in the synthesis of surface impedance patterns. One advantage of using holographic structures is their multibeam radiation property without the need for a complex feeding network. For this purpose, the superposition of desired beams should be used in the synthesis of holograms [21]. Holograms can be used in the realization of multifunctional radiators, which use a single aperture to generate separate beams [22]. In Ref. [23], the signal multiplexing property from a 2D hologram is discussed. Leaky-wave holograms can be classified into two types of isotropic and anisotropic structures, based on their unit-cell shape. Isotropic holograms are only capable of synthesizing the wave front direction. However, polarization control with high purity level is difficult to realize. In communication systems it is

_____

[*]amini_am@elec.iust.ac.ir

[†]h_oraizi@iust.ac.ir

[‡]mhamedani7714@yahoo.com

[§]keivaan.ali@gmail.com

important to achieve polarization purity in order to prevent unwanted interference, especially in systems using two orthogonal polarizations to generate simultaneously two communication channels at the same frequency [24,25].

In Ref. [26], the polarization conversion with isotropic structures was investigated. In this reference, by properly modifying the phase of field in the aperture, the desired polarization was obtained. However, the phase modification method was only suitable for polarization control over the design angle and the cross-polarization component significantly arises at other angles. This issue is discussed in more detail in the following.

In anisotropic holograms, the wave front polarization can be readily controlled, compared with the isotropic holograms. Recently, synthesis methods of these structures that achieve more degrees of freedom have received considerable attention. In Ref. [27], the generalized holography method was proposed for the synthesis of anisotropic metasurfaces. In Ref. [28] this method has been used to manipulate dual beams with different polarizations. Meng *et al.* [29] demonstrated that the linearly polarized vortex beam in the microwave regime can be obtained using the generalized holography method. In general, the holography theory is considered as a synthesis method and requires full-wave analysis for the validation of implemented structures. Owing to the fact that such antennas are composed of structures with dimensions of several wavelengths, their numerical full-wave analysis is very time consuming. To reduce the simulation time, the method of moments (MoM) using the Gaussian ring [30] and Fourier-Bessel [31] basis functions have been developed in the literature. The MoM framework is based on the discrete expansion of the unknown surface current density in terms of basis functions and the calculation of unknown coefficients. However, computing the tensorial Green's functions and dealing with spectral singularities have increased the complexity of analysis.

In this paper, a systematic approach based on the aperture field estimation (AFE) technique [32] and Fourier optics [33,34] is proposed. The AFE theory is extended for the accurate prediction of the far-zone wave front, generated by anisotropic holograms. The advantage of using this method is that it can predict the amplitude and phase properties of the radiation pattern without the need for full-wave simulation, which greatly reduces the synthesis and optimization time consumption. Two different examples are presented to investigate the significance of the proposed method. In the first example, an anisotropic hologram is designed to generate a vertically polarized pencil beam. In this case, a high directivity all over the bandwidth is obtained. In the synthesis of vertically polarized holograms, two points are considered: (1) achieving the desired polarization purity across the visible region; (2) attaining frequency scanning in the desired bandwidth. In general, the polarization purity is required not only

at the desired angle, but also at other angles to prevent unwanted interference with other radiation sources. The desired purity of cross-polarization depends on the sensitivity of the receiver and its application. However, in the antenna engineering, it is desirable to maximize the co- to cross-polarization ratio.

In the second example, an anisotropic hologram for perfect conversion of a linearly polarized surface wave into a circularly polarized vortex beam is proposed. Various methods for the generation of electromagnetic waves carrying orbital angular momentum (OAM) modes have been reported. Circular arrangement of phased array antennas [35], reflect arrays [36], transmit arrays [37], and annular-shape traveling-wave antennas [38] are common approaches for OAM generation. Owing to the feed network complexity and the destructive effects of mutual couplings among the elements, the implementation of phased array antennas reduces their efficiency. In reflect arrays and transmit arrays, the feed network is placed outside the structure and makes it bulky and unsuitable for integration. Leaky-wave holograms can resolve these issues, as their feeds are embedded in the vicinity of impedance surface and they do not need any phase shifters or complex feed networks.

II. HOLOGRAPHY PRINCIPLE AND APERTURE FIELD ESTIMATION METHOD

Based on the holography principle, an arbitrary wave front (object wave) can be recovered from an interferogram, which records the interference of object and reference waves [39]. In the leaky-wave structures, the reactive impedance surfaces (RISs) play the role of interferograms, which are formed from the interference patterns [20]. In general, the relation of scalar surface impedance and recorded waves, can be written as follows [27]:

$$Z_s(x,y) = jX_0\{1 + M \times \text{Re}[\psi_{\text{ref}}(x,y)\psi_{\text{obj}}^*(x,y)]\}, \quad (1)$$

where ψ_{ref} and ψ_{obj} represent the reference and object waves, respectively. Here X_0 is the average surface impedance and M is the modulation factor. The reference wave can be planar ($e^{-jk_x x}$) [40] or cylindrical ($e^{-jk_\rho \rho}$) [27]. In both cases, the amplitude of the wave function is 1. The more precise version of cylindrical surface wave can be treated as a Hankel function [$H_1^{(2)}(k_\rho \rho)$]. In this case, the decay of surface wave in the propagation direction is taken into account. In this paper, the cylindrical reference-wave function is defined in its more accurate form (the Hankel function). It is worth noting that, in the asymptotic form of the reference wave, the magnitude of wave decays with the factor of $(1/\sqrt{\rho})e^{-\alpha_\rho \rho}$. Figure 1 shows the hologram structure including reference-wave generator and impedance metasurface, which produce the object wave at the desired direction. Equation (1) emphasizes
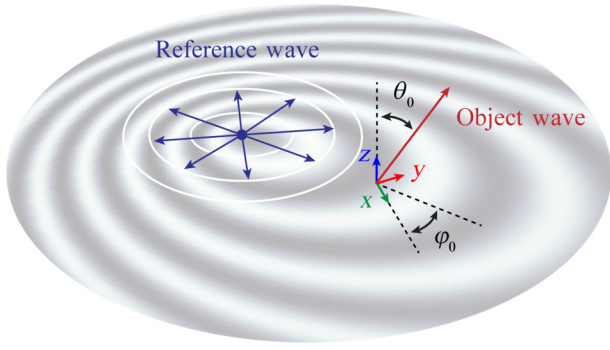
FIG. 1.   Conceptual structure of the hologram including reference wave and modulated metasurface for generating an object wave in the desired direction.

that, to have the desired wave function in the hologram aperture, the level of impedance should be modulated in the spatial domain. Equation (1) is valid for isotropic surface impedances, which synthesizes the phase of object wave front. However, isotropic holograms are not capable of controlling the wave polarization. For this purpose, it is necessary to generalize the holography formulation for anisotropic structures, as [41]

$$\bar{\bar{Z}}_s \cdot \hat{\rho} = jX_0 \left[\hat{\rho} + 2\mathrm{Im}\left(\frac{\vec{E}_a}{\hat{\phi} \cdot \vec{H}_t|_{z=0^+}} \right) \right], \qquad (2)$$

where $\vec{H}_t$ is the tangential magnetic field on the aperture, generated by the cylindrical surface-wave source. According to the principle of energy conservation, the impedance $\bar{\bar{Z}}_s$ is an anti-Hermitian tensor (i.e., $\bar{\bar{Z}}_s^{\dagger} = -\bar{\bar{Z}}_s$) and can be written as follows:

$$\bar{\bar{Z}}_s = Z_{\rho\rho}\hat{\rho}\hat{\rho} + Z_{\phi\phi}\hat{\phi}\hat{\phi} + Z_{\rho\phi}(\hat{\rho}\hat{\phi} + \hat{\phi}\hat{\rho}). \qquad (3)$$

Note that the reciprocity emphasizes that the tensor should be symmetrical and purely imaginary [42]. The vector $\vec{E}_a$ is the object electric field and possesses the general form of

$$\vec{E}_a(x,y) = E_{ax}(x,y)\hat{x} + E_{ay}(x,y)\hat{y}. \qquad (4)$$

The aperture field and far-zone field are related as [33]

$$\vec{E}_F(r,\theta,\phi) \approx \frac{jke^{-jkr}}{2\pi r}\left[F_\theta(\theta,\phi)\hat{\theta} + F_\phi(\theta,\phi)\hat{\phi} \right], \qquad (5)$$

$$F_\theta(\theta,\phi) = f_x \cos\phi + f_y \sin\phi, \qquad (6)$$

$$F_\phi(\theta,\phi) = \cos\theta(-f_x \sin\phi + f_y \cos\phi), \qquad (7)$$

where f_x and f_y are the Fourier spectrums of E_{ax} and E_{ay}, respectively and can be expressed as

$$f_x(k_x,k_y) = \iint_{ap} E_{ax}(x',y',z'=0)e^{j(k_xx'+k_yy')}\,dx'\,dy', \qquad (8)$$

$$f_y(k_x,k_y) = \iint_{ap} E_{ay}(x',y',z'=0)e^{j(k_xx'+k_yy')}\,dx'\,dy'. \qquad (9)$$

The above integrations are applied on the aperture area of the hologram. In Eq. (2), E_{ax} and E_{ay} may be chosen independently with arbitrary forms. This shows that the manipulation of polarization by anisotropic structures is easily possible. For example, to achieve vertical polarization, the azimuthal component of the far-zone field (F_ϕ) must be zero. In addition, for circular polarization, the required condition is

$$F_\phi(\theta_0,\phi_0) = \pm jF_\theta(\theta_0,\phi_0). \qquad (10)$$

III. DESIGN EXAMPLES

In this section, different holograms with the AFE method are designed to generate planar and helical wave fronts. Without loss of generality, the operating frequency is assumed to be 18 GHz. For the pencil beam, all of the holograms radiate vertically polarized waves in a tilted direction at $\theta = 30°$ and $\phi = 0°$. For the vortex beam, the holograms are supposed to radiate at the broadside direction. In this section, the AFE method is extended for both isotropic and anisotropic structures. The aim of this section is to show the capability of this method for the design of holographic antennas with arbitrary phase and polarization.

A. Pencil beam pattern synthesis

1. Isotropic hologram

As a first example, the conventional center-fed isotropic hologram has been analyzed by the AFE method. This hologram suffers greatly from the null in the designed direction. In this section, we expand the AFE method to provide an explanation of this issue. For the center-fed isotropic holograms, the magnetic field produced by the launcher can be expressed as a Hankel function:

$$H_\phi = -J_{\mathrm{sw}}H_1^{(2)}(k_{\mathrm{sw}}\rho), \qquad (11)$$

where $k_{\mathrm{sw}} = \beta_{\mathrm{sw}} - j\alpha_{\mathrm{sw}}$ is the surface-wave number. The asymptotic form of Hankel function is

$$H_1^{(2)}(k_{\mathrm{sw}}\rho) \approx \sqrt{\frac{2}{\pi\sqrt{\beta_{\mathrm{sw}}^2 + \alpha_{\mathrm{sw}}^2}\rho}}je^{-j(k_{\mathrm{sw}}\rho - \zeta_0)}, \qquad (12)$$

where ζ_0 is a function of α_{sw} and β_{sw}. Therefore, the surface impedance becomes

$$\bar{\bar{Z}}_s \cdot \hat{\rho} = jX_0 \left[\hat{\rho} + \frac{\sqrt{2\pi \sqrt{\beta_{sw}^2 + \alpha_{sw}^2} \rho}}{J_{sw}} \times \text{Im} \left(\vec{E}_a j e^{j(k_{sw}\rho - \zeta_0)} \right) \right]$$

(13)

Being isotropic imposes that the electric field should have only the ρ component. Hence, E_{ax} and E_{ay} must be

$$E_{ax} = E_0(\rho) e^{-jk_0(x\sin\theta_0\cos\phi_0 + y\sin\theta_0\sin\phi_0)} \cos\phi,$$ (14)

$$E_{ay} = E_0(\rho) e^{-jk_0(x\sin\theta_0\cos\phi_0 + y\sin\theta_0\sin\phi_0)} \sin\phi,$$ (15)

where θ_0 and ϕ_0 are vertical and horizontal angles of propagation vector $\vec{k}$ (see Fig. 1). After more simplifications, we obtain

$$Z_s = jX_0[1 + M_0(\rho) \times \cos(\beta_{sw}\rho - k_0 x\sin\theta_0\cos\phi_0$$
$$- k_0 y\sin\theta_0\sin\phi_0 - \zeta_0)],$$ (16)

where

$$M_0(\rho) = E_0(\rho) \frac{\sqrt{2\pi \sqrt{\beta_{sw}^2 + \alpha_{sw}^2} \rho}}{J_{sw}} e^{\alpha_{sw}\rho}.$$ (17)

In conventional isotropic holograms, the parameter M is independent of ρ, which gives

$$E_0(\rho) = M \frac{J_{sw}}{\sqrt{2\pi \sqrt{\beta_{sw}^2 + \alpha_{sw}^2} \rho}} e^{-\alpha_{sw}\rho}.$$ (18)

Equation (18) shows that if M is constant, the aperture field magnitude attenuates with the factor of $(1/\sqrt{\rho})e^{-\alpha_{sw}\rho}$. Both X_0 and M are the two degrees of freedom in the design, yet there are limits in determining their values. The parameter X_0 has to be chosen such that the impedance range can be synthesized easily. The parameter M is inversely proportional to the antenna directivity, that is, for lower values of M, the directivity is higher and vice versa [40]. Here, it is desirable to calculate the far-zone pattern at $\theta = \theta_0$ and $\phi = \phi_0$. Using (14) and (15) in (6) and (7) leads to

$$F_\theta(\theta_0, \phi_0) = \int_{-a/2}^{a/2} \int_{-b/2}^{b/2} E_0(\rho') \cos(\phi' - \phi_0) \, dx' \, dy',$$

(19)

$$F_\phi(\theta_0, \phi_0) = \cos\theta_0 \int_{-a/2}^{a/2} \int_{-b/2}^{b/2} E_0(\rho') \sin(\phi' - \phi_0) \, dx' \, dy',$$

(20)

where $\rho' = \sqrt{x'^2 + y'^2}$ and $\phi' = \tan^{-1}(y'/x')$. Owing to the structure symmetry, the above integrations lead to zero.
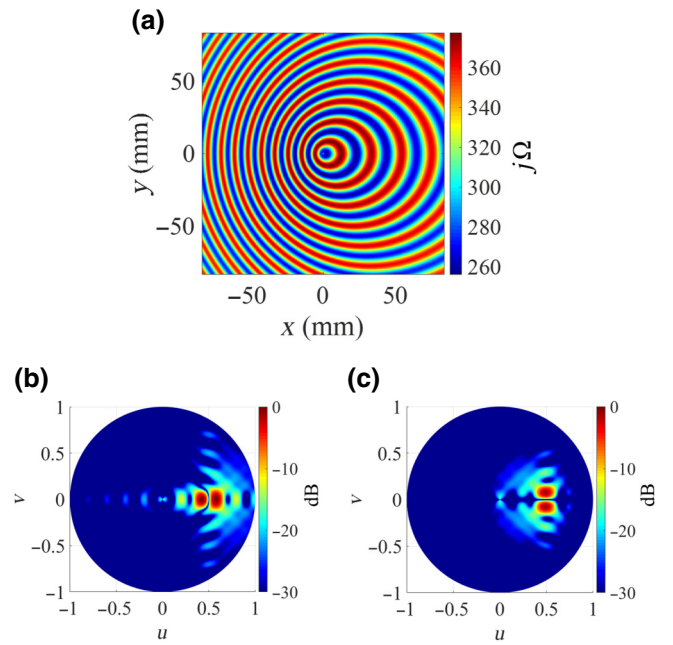

FIG. 2. Surface impedance and radiation patterns of a conventional isotropic hologram: (a) synthesized impedance pattern; (b) vertical component of the pattern (F_θ); and (c) horizontal component of the pattern (F_ϕ).

This indicates that a null appears at $\theta = \theta_0$ and $\phi = \phi_0$, which is the desired direction of propagation. Figure 2 shows the impedance surface and far-zone patterns of the conventional isotropic hologram. Parameters M and X_0 in Eq. (16) are chosen as 0.2 and $0.84\eta_0$, respectively. Here η_0 is the wave impedance in free space and is equal to 376.7 Ω. These values are selected regarding the available technology in our laboratory, in order for the antenna to be synthesized by the grounded patch unit cells. All of the patterns are plotted in the u–v plane ($u = \sin\theta\cos\phi$, $v = \sin\theta\sin\phi$) and normalized to the maximum value of vertical component (F_θ). When the feed is located in the center of hologram a null in the object wave direction can be observed. This is due to the destructive effect of the backward leaky mode, which can be eliminated by the phase correction of the aperture field [26,43]. The 180° phase shift in the aperture field corresponding to the part generating the backward mode, compensates its destructive effect. In this case both the forward and backward modes have constructive effects on the far-zone field. Thus, the ρ component of electric field can be modified as follows:

$$E_{a\rho} = E_0(\rho) e^{-jk_0[x\sin\theta_0\cos\phi_0 + y\sin\theta_0\sin\phi_0 + \pi u(-x)]},$$ (21)

where $u(x)$ is unit step function. The impedance and far-zone patterns of phase-compensated isotropic hologram are drawn in Fig. 3. Observe that the pattern is improved significantly compared with the conventional
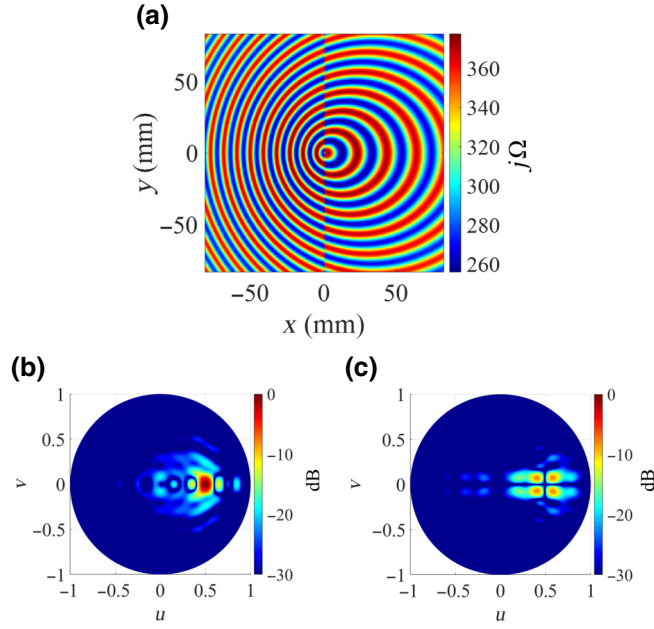
(a)

FIG. 3. Surface impedance and radiation patterns of a phase-compensated isotropic hologram: (a) synthesized impedance pattern; (b) vertical component of the pattern (F_θ); and (c) horizontal component of the pattern (F_ϕ).

case. However, the cross-polarization in the u–v plane (F_ϕ) is inappropriate.

2. Anisotropic hologram

Isotropic holograms can only synthesize the wave front direction and no control can be attained over the polarization of leaky mode. For anisotropic holograms, however, the aperture field components can be defined independently. For example, if the aim is to synthesize the antenna with vertical polarization at the direction of $\theta = \theta_0$ and $\phi = \phi_0$, the horizontal components of the far-zone field (F_ϕ) should be set to zero. Hence,

$$F_\phi(\theta_0, \phi_0) = 0, \tag{22}$$

$$f_y = f_x \tan\phi_0. \tag{23}$$

Therefore, the aperture components can be expressed as

$$E_{ax} = E_0(\rho)e^{-jk_0(x\sin\theta_0\cos\phi_0 + y\sin\theta_0\sin\phi_0)}\cos\phi, \tag{24}$$

$$E_{ay} = E_{ax}\tan\phi_0. \tag{25}$$

Using (11), (24), and (25) in (2), the tensor components can be derived as

$$Z_{\rho\rho} = jX_0[1 + M\cos\phi \times \sin(\beta_{sw}\rho - k_0 x\sin\theta_0\cos\phi_0 \\ - k_0 y\sin\theta_0\sin\phi_0 - \zeta) \times (\cos\phi + \tan\phi_0\sin\phi)], \tag{26}$$

$$Z_{\rho\phi} = jX_0[M\cos\phi \times \sin(\beta_{sw}\rho - k_0 x\sin\theta_0\cos\phi_0 \\ - k_0 y\sin\theta_0\sin\phi_0 - \zeta) \times (\tan\phi_0\cos\phi - \sin\phi)]. \tag{27}$$

Note that $Z_{\phi\phi}$ has a very small effect on the synthesis of the aperture field, which is due to the TM-like surface-wave excitation [41]. Figure 4 shows the computed impedances and far-zone patterns of a center-fed anisotropic hologram. The values of modulation factor (M) and average impedance (X_0) are selected equal to 0.2 and $0.84\eta_0$, respectively. As can be seen from Fig. 4(d), the cross-polarization component of far-zone pattern is reduced significantly compared with the isotropic case [see Fig. 2(c)]. This improvement occurs at all points of the u–v plane (namely the visible region). The improvement in the level of cross-polarization can be explained as follows. Equation (25) indicates that the orientation of the aperture field is always in the ϕ_0 direction. That is, in anisotropic structures, the impedance surfaces perform two functions: one is to direct the leaky-wave propagation along the spatial angles ϕ_0 and θ_0 and the other is to redirect the aperture electric field vector along the ϕ_0 direction. In our example, the value of $\phi_0 = 0$ is chosen. Therefore, the y component of aperture field will be always zero and as a result, f_y will be zero. From Eqs. (6) and (7) it can be deduced that the ratio of the co- to cross-polarization components is simplified as follows:

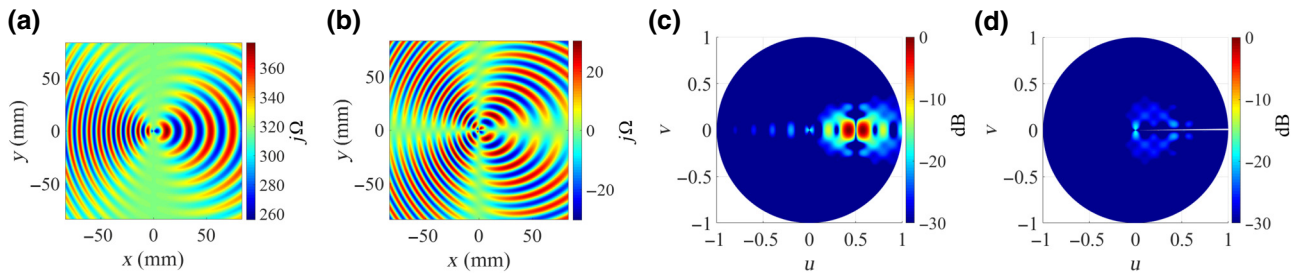$$\left|\frac{F_\theta}{F_\phi}\right| = \left|\frac{\cot\phi}{\cos\theta}\right|. \tag{28}$$

FIG. 4. Surface impedance and radiation patterns of a conventional anisotropic hologram: (a) $X_{\rho\rho}$; (b) $X_{\rho\phi}$; (c) vertical component of the pattern (F_θ); and (d) horizontal component of the pattern (F_ϕ).
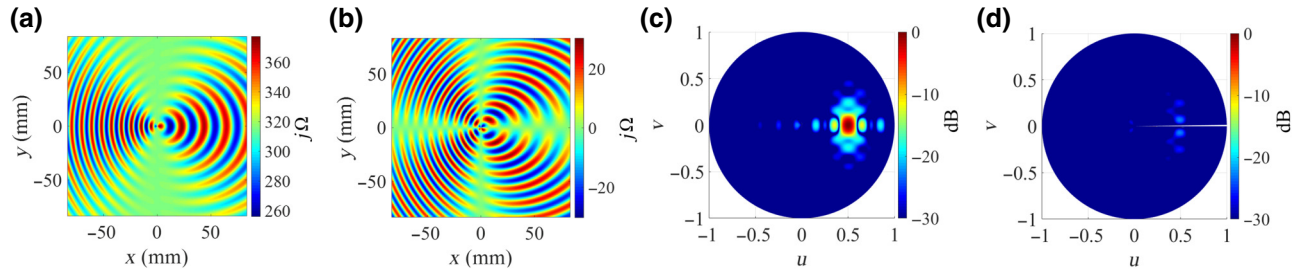
FIG. 5. Surface impedance and radiation patterns of phase-compensated anisotropic hologram: (a) $X_{\rho\rho}$; (b) $X_{\rho\phi}$; (c) vertical component of the pattern (F_θ); and (d) horizontal component of the pattern (F_ϕ).

If we measure the ratio of co- to cross-polarization components in the vicinity of the design angle (for example, $\delta\phi$), owing to the small amount of $\delta\phi$, the magnitude of the ratio is still sufficiently large and acceptable. Equation (28) shows that by getting away from the design angle (increasing $\delta\phi$) the ratio of co- to cross-polarization components will decrease. Considering the fact that the co-polarization component will decrease by increasing $\delta\phi$, the cross component will also have a suitable level. For further investigations, consider the example in Fig. 4. At $\theta = 30°$, the ideal co- to cross-polarization ratio at $\delta\phi = 0, 5$, and $10°$ are infinite, 22 dB, and 16 dB, respectively, which are the desired values.

Owing to the destructive effects of backward mode, as in the conventional isotropic hologram, the null occurs exactly in the desired direction. In order to remove the null, the phase of aperture field should be corrected, according to the following equations:

$$E_{ax} = E_0 e^{-jk_0[x\sin\theta_0\cos\phi_0 + y\sin\theta_0\sin\phi_0 + \pi u(-x)]}, \quad (29)$$

$$E_{ay} = E_0 e^{-jk_0[x\sin\theta_0\cos\phi_0 + y\sin\theta_0\sin\phi_0 + \pi u(-x)]}\tan\phi_0. \quad (30)$$

Figure 5 depicts the impedance and far-zone patterns of a phase-compensated anisotropic hologram. It is clear that the radiated pattern is null-free in the desired direction and the cross-polarization level is appropriate.

3. Reflector-based anisotropic hologram

In center-fed holograms, both the forward and backward modes contribute to the radiation. Assume that the hologram is designed to generate an object wave in the inclined direction of $\theta = \theta_0$ at frequency f_0. By increasing the frequency, the forward mode angle moves away from the broadside, and the backward angle approaches to the broadside apex. This variation of angles of the forward and backward modes deteriorates the total radiated beam. Figure 6(a) represents the direction of forward and backward leaky waves at f_0 and $f_0 + \delta f$. It is clear that, the forward and backward leaky modes move away from each other at $f_0 + \delta f$. To eliminate the destructive effect of the backward mode, a perfect electric conductor (PEC) wall reflector can be employed [see Fig. 6(b)].

The reflector confines the surface wave inside the forward region and orients the backward leaky mode into the forward one, leading to the improvement of the radiation pattern [44,45]. In the presence of the surface-wave reflector, the magnetic field in Eq. (2) does not follow the Hankel function. In this case, the total field will be obtained from the sum of incident and reflected fields from the reflector. The best method for such computations, is the use of COMSOL MULTIPHYSICS [46]. Figure 7 shows the field distribution of current source in the vicinity of
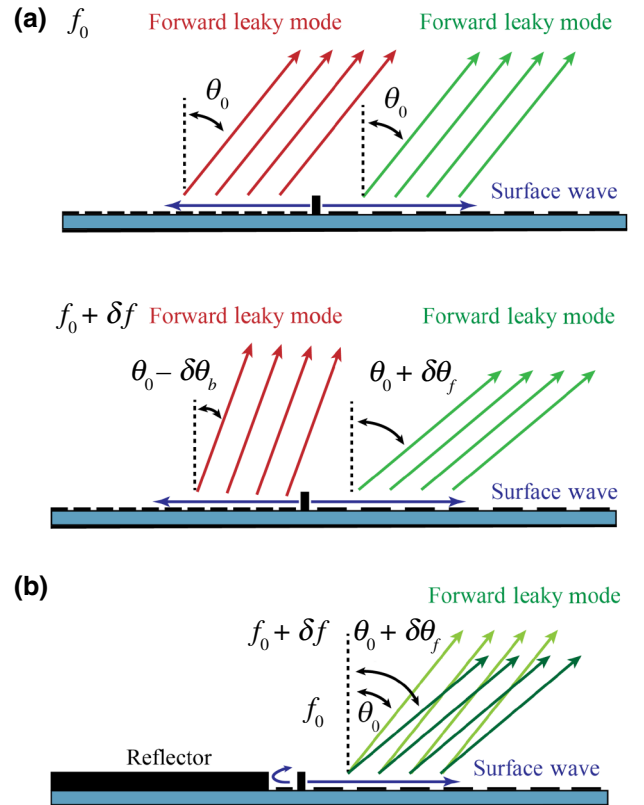

FIG. 6. (a) Schematic of forward and backward leaky mode behavior in the center-fed hologram at frequencies f_0 and $f_0 + \delta f$. (b) The process of backward mode redirection for improvement of radiation characteristics.
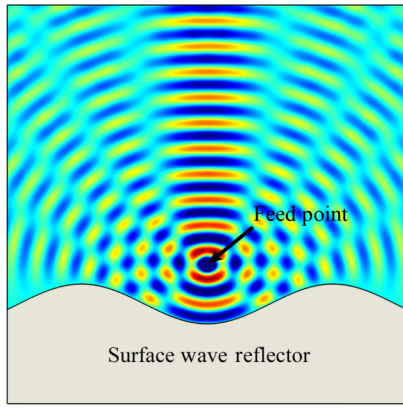
FIG. 7. The distribution of electric field in the vicinity of an arbitrary shaped PEC wall.

FIG. 9. Radiation patterns of reflector-based holograms in Fig. 8: (a),(b) isotropic hologram; (c),(d) anisotropic hologram.

an arbitrary shaped PEC reflector. Note that the simulation is performed in a medium with effective refractive index of $n = \sqrt{1 + (X_0/\eta_0)^2}$, which is seen by the reference wave. The effective refractive index models the presence of metasurface in the computations. In this problem, by implementing the reflector, the half space in $x < 0$ is removed. The current source, however, is near enough to the reflector to minimize the destructive effects of backward modes. Moreover, the current source should not be very close to the reflector to prevent the fabrication problems. Regarding the above considerations, the distance between the source and the reflector is chosen as 3 mm. Figure 8 shows the impedance patterns of isotropic and anisotropic holograms in the presence of a PEC wall. The modulation factor and average impedance are selected as $M = 0.2$ and $X_0 = 0.84\eta_0$, respectively. The desired radiation angles are $\theta_0 = 30°$ and $\phi_0 = 0°$. The calculated co- and cross-polarization patterns are drawn in Fig. 9. It is clear that, by using the anisotropic unit cells, the cross-polarization component is improved significantly. It should be mentioned that the periodicity of impedance variations is basically smaller than the forward section. In order to synthesize the impedance surfaces of backward section, it
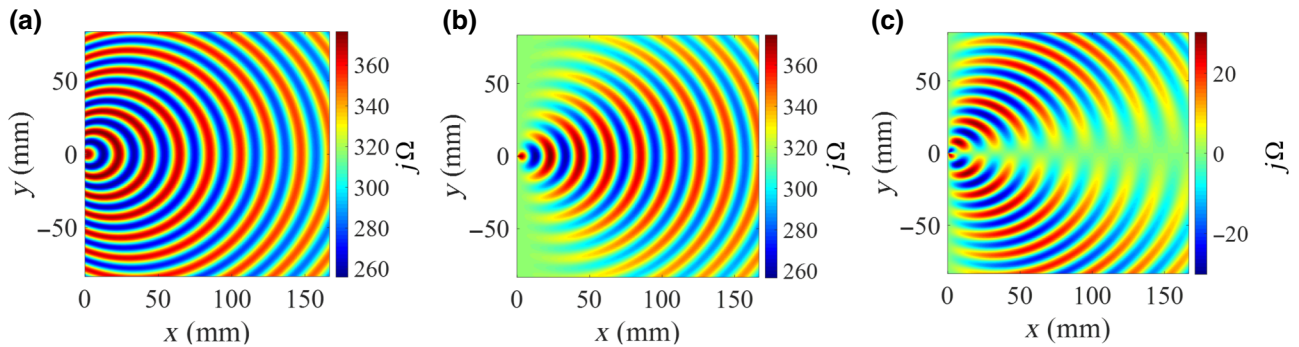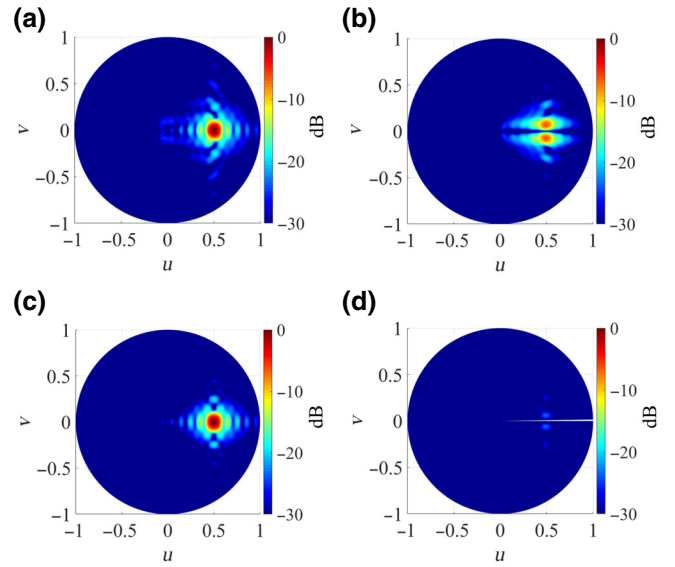
is required to design unit cells with smaller dimensions for favorable resolution. Clearly, decreasing the resolution of synthesized impedance surface, increases the rate of error. In practice, the miniaturization of unit cells requires the use of substrates with higher permittivity, which decreases the bandwidth [47]. Considering the above points, the elimination of the backward mode and the use of a reflector is preferable for low-profile structures.

B. Vortex-beam synthesis

1. Isotropic hologram

As the vortex beam with topological charge of l has an azimuthal phase dependency ($e^{-jl\phi}$) [48], the general form of aperture fields can be considered as follows:

$$E_{ax} = E_0(\rho)e^{-jk_0(x\sin\theta_0\cos\phi_0 + y\sin\theta_0\cos\phi_0)}e^{-jl\phi}\cos\phi, \quad (31)$$

$$E_{ay} = E_0(\rho)e^{-jk_0(x\sin\theta_0\cos\phi_0 + y\sin\theta_0\cos\phi_0)}e^{-jl\phi}\sin\phi. \quad (32)$$

FIG. 8. Surface impedance patterns of reflector-based holograms: (a) isotropic hologram; (b),(c) anisotropic hologram.
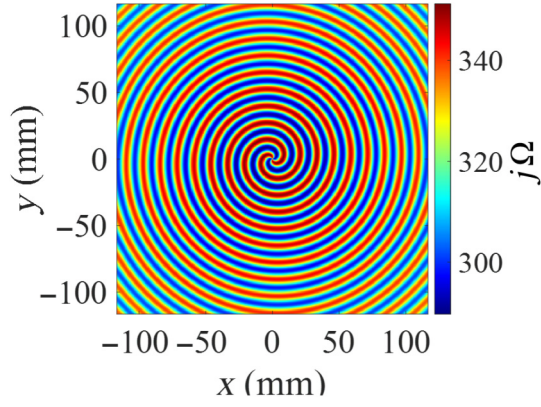
FIG. 10. Scalar surface impedance distribution for generating vortex-beam with topological charge of $l = 2$.

It can be readily proved that if l is an integer number, then the term $e^{-jl\phi}$ appears in its Fourier transform and as a consequence in F_θ and F_ϕ (see Ref. [49]). If the parameter M has a constant value, we can consider the amplitude of $E_0(\rho)$ similar to Eq. (18). As the electric field vector only has the radial component, the synthesized impedance surface is isotropic. Figure 10 shows the synthesized surface impedance to generate vortex beam with topological charge of $l = 2$. The beam orientation angle is chosen as $\theta_0 = 0°$ and $\phi_0 = 0°$. The magnitude and phase of the far-zone pattern are plotted in Fig. 11. The results show that the ϕ component of the electric field is carrying OAM mode with the topological charge of $l = 2$. The null created in the amplitude is related to the phase singularity [1]. Figure 11(a) shows that part of power exists in F_θ. However, the amount of power shared between the two components cannot be controlled.

2. Anisotropic hologram

Now the approach of generating OAM mode with circular polarization using an anisotropic hologram is investigated. The condition for creating circular polarization is as follows:

$$F_\phi(\theta_0, \phi_0) = \pm j F_\theta(\theta_0, \phi_0), \tag{33}$$

where $+$ and $-$ denotes left-hand and right-hand polarizations, respectively. If the orientation angle is considered to be broadside ($\theta_0 = 0°$ and $\phi_0 = 0°$), the aperture field spectrum can be written as

$$f_y = \pm j f_x. \tag{34}$$

According to Eqs. (6) and (7), the far-zone components can be obtained as follows:

$$F_\theta(\theta, \phi) = f_x \cos \phi \pm j f_x \sin \phi = f_x e^{\pm j\phi}, \tag{35}$$
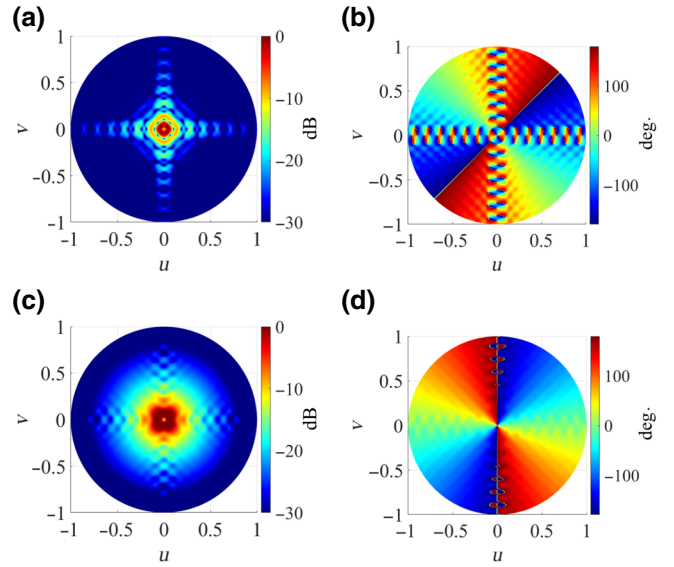

FIG. 11. Radiation patterns of the isotropic hologram in Fig. 10: (a) amplitude of the θ component; (b) phase of the θ component; (c) amplitude of the ϕ component; (d) phase of the ϕ component.

$$F_\phi(\theta, \phi) = \cos \theta (-fx \sin \phi \pm j f_x \cos \phi) = \pm j \cos \theta f_x e^{\pm j\phi}. \tag{36}$$

Observe that the term $e^{\pm j\phi}$ is added to both the θ and ϕ components owing to the condition for circular polarization. If we want to eliminate this term, we should add the term $e^{\mp j\phi}$ to the aperture field. According to the above considerations, E_{ax} and E_{ay} can be defined as follows:

$$E_{ax} = E_0(\rho) e^{-j(l\pm 1)\phi}, \tag{37}$$

$$E_{ay} = \pm j E_{ax}. \tag{38}$$

In Fig. 12 the components of $X_{\rho\rho}$ and $X_{\rho\phi}$ for the topological charge of $l = 2$ are illustrated. Figures 13(a)–13(d) show the θ and ϕ components of a far-zone pattern, respectively. It can be seen that the power is shared equally between the two orthogonal components. As expected, the number of wave front twists is equal to 2.

IV. HOLOGRAM SYNTHESIS

In the previous examples, the isotropic and anisotropic impedance surfaces are used for the synthesis of holograms. Practically, such impedance patterns need to be realized. This section describes the process of synthesis by the periodic structures.

A. Isotropic impedance surfaces

Leaky-wave holographic antennas are implemented based on surface-wave waveguides. These waveguides
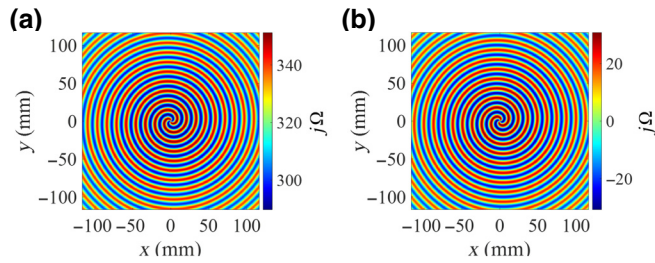
FIG. 12. Surface impedance patterns for generating a circularly polarized vortex beam with topological charge of $l = 2$: (a) $X_{\rho\rho}$; (b) $X_{\rho\phi}$.

support TM-like, TE-like, or hybrid modes, which are composed of both TM and TE components. In the isotropic surface, the TE-like mode or TM-like mode is dominant. Note that, in TM-like mode, the magnetic field only has the transversal components in the propagation direction. Based on duality, the same definition can be applied to TE-like mode and the electric field. For surface waveguide, the boundary condition for the fields can be defined as follows:

$$E_t|_{z=0^+} = \bar{\bar{Z}}_s \cdot \hat{z} \times H_t|_{z=0^+}, \tag{39}$$

where $\bar{\bar{Z}}_s$ is the impedance tensor and $\hat{z}$ is the unit vector, which is perpendicular to the surface. For the isotropic surface, which supports TM-like mode, the impedance has a

scalar parameter (Z_s) and can be obtained as follows:

$$Z_s = \frac{j\alpha_z}{\omega\epsilon_0} = j\frac{\sqrt{(k_x^2 + k_y^2) - k_0^2}}{\omega\epsilon_0}, \tag{40}$$

where α_z indicates the attenuation constant of the wave above the surface. Grounded dielectric slabs can act as TM mode waveguides [50]. However, in order to have proper control over the impedance, we need to place periodic patches on the grounded slabs. The patch geometry and unit-cell dimensions should be chosen suitably to provide the required impedance range. Square [27], circular [51], and hexagonal patches [44] are common geometrical shapes for the synthesis of isotropic impedance surfaces. In general, the dimensions of a unit cell are usually chosen between $\lambda/10$ and $\lambda/5$ (see Refs. [21,47]). In this situation, these pixels can effectively model the impedance surface. If the dimensions are larger than $\lambda/5$ (especially, when they approach $\lambda/2$), these patches act as local resonators. Note that, for the value of $\lambda/2$, the first-order dipolar resonance occurs, where patches radiate effectively. In this paper, the square patch is selected to construct the isotropic hologram. The dimensions of square lattice are selected as 2.8×2.8 mm^2, which is equal to $\lambda/6$ at the design frequency (18 GHz). Rogers RO4003 (with permittivity 3.55 and thickness 1.524 mm) is chosen for the substrate. Note that, if the unit cell is miniaturized further, its surface impedance decreases and therefore the required range cannot be covered. The substrate with a higher permittivity can also be used to miniaturize the unit cell. However, increasing substrate permittivity reduces the operational bandwidth of the hologram [47].

B. Isotropic impedance retrieval

As mentioned in the previous section, for surfaces that support TM-like mode, the value of impedance can be obtained from Eq. (40). In order to calculate the
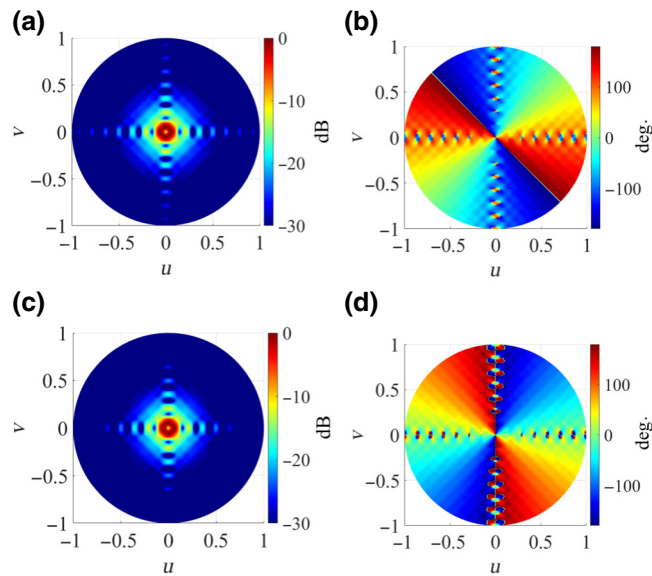

FIG. 13. Radiation patterns of an anisotropic hologram in Fig. 12: (a) amplitude of the θ component; (b) phase of the θ component; (c) amplitude of the ϕ component; (d) phase of the ϕ component.
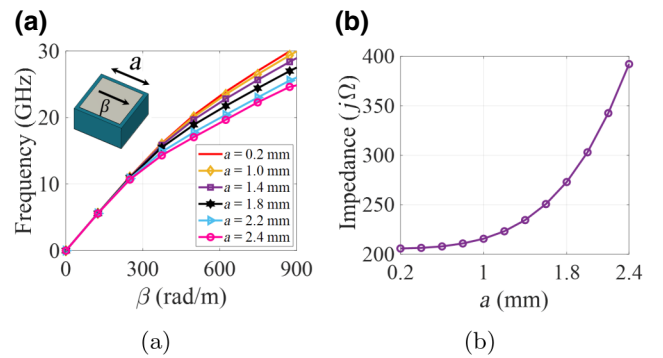

FIG. 14. Simulation results of the proposed unit cell for the case of $k_x = \beta$ and $k_y = 0$: (a) the dispersion curves for different sizes of patch; (b) the curve of variation of scalar impedance at 18 GHz.
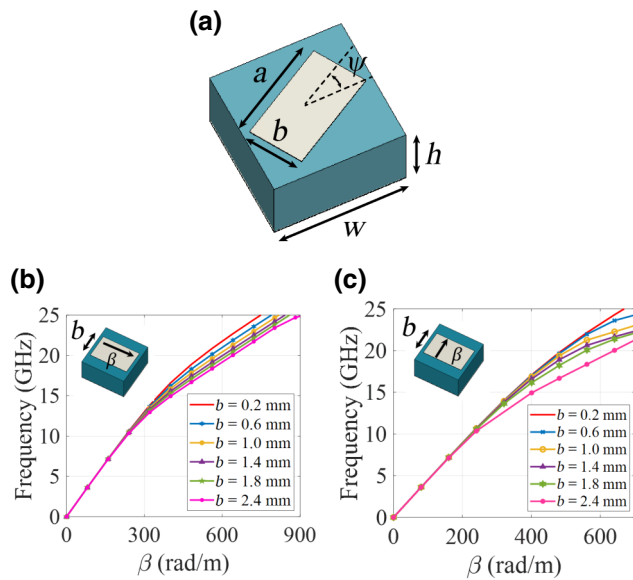
FIG. 15. (a) Proposed unit cell for realization of anisotropic impedance. The period of lattice is $w = 2.8$ mm and the width of patch changes from 0.2 to 2.4 mm. The parameter ψ indicates the rotation angle of patch relative to the propagation direction. (b) Variation of the dispersion curve for different widths of patch when the wave propagates along the x axis ($k_x = \beta$ and $k_y = 0$). (c) Variation of the dispersion curve for different widths of patch when the wave propagates along the y axis ($k_x = 0$ and $k_y = \beta$).

FIG. 16. Impedance map of the proposed unit cell in Fig. 15(a): (a) $X_{\rho\rho}$; (b) $X_{\rho\phi}$.

impedance, it is necessary to extract x and y components of propagation vector (k_x and k_y) using the eigenmode solver. Assuming that the unit cell is isotropic, the direction of propagation can be arbitrarily chosen. Figure 14(a) shows the dispersion diagram of the proposed unit cell by varying the length of the square patch (namely a). In Fig. 14(b) the impedance variation with respect to the length of patch is plotted.

C. Anisotropic impedance surfaces

Similar to the isotropic unit cells, anisotropic unit cells should also be smaller than $\lambda/5$ in order to effectively
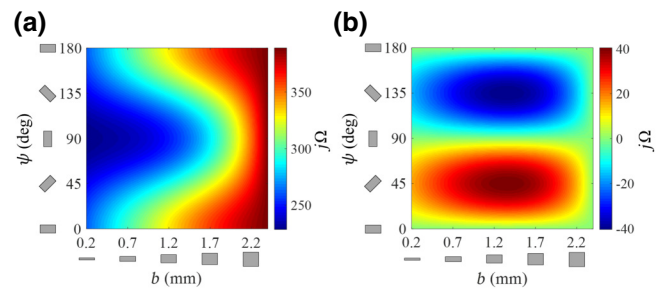
model the impedance surface. Furthermore, the patch geometry should possess axial asymmetry to have tensorial impedance [41]. The geometry of the patch determines its impedance value and degree of anisotropy. In choosing the shape of patches, the following points should be considered [47]: (1) anisotropy control; (2) the range of impedance variations; (3) the operation bandwidth of the unit cell; (4) the sensitivity of the fabrication error; (5) losses in the metal. Various shapes have been suggested in the literature. For example, the "coffee bean" shapes [41] are relatively insensitive to the fabrication tolerance, but their operational bandwidth is limited. The "double anchor" and "double pi" shapes [47] have favorable bandwidth and present a wide range of impedance. However, their losses are high, which affect the total efficiency of the hologram. The rectangular and elliptical patches have acceptable bandwidth and are relatively insensitive to the fabrication tolerance. According to the above considerations, the rectangular patch with a square lattice is chosen.

D. Anisotropic impedance retrieval

Figure 15(a) demonstrates the proposed anisotropic unit cell with a rectangular patch. Two parameters are considered for changing the impedance of the patch: the width
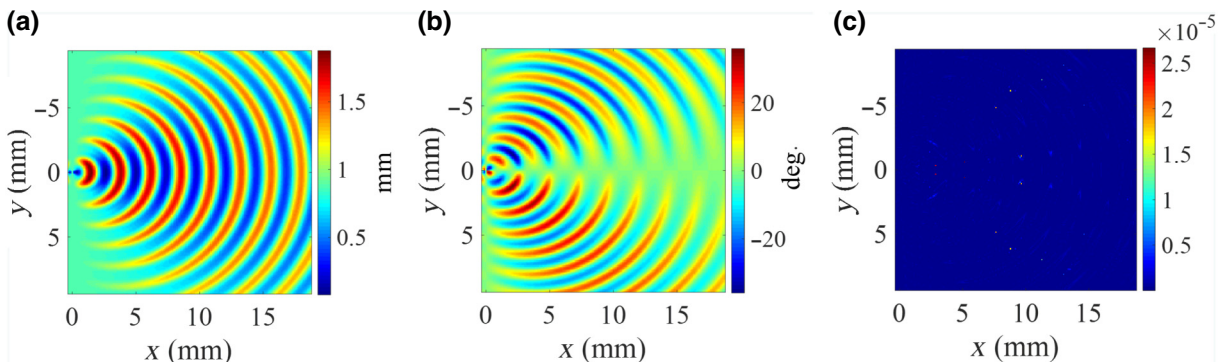

FIG. 17. Required dimensions for the realization of the impedance patterns in Figs. 8(b) and 8(c); (a) width of the patch [b (mm)]; (b) rotation angle of the patch [ψ (deg)]; (c) calculation error.
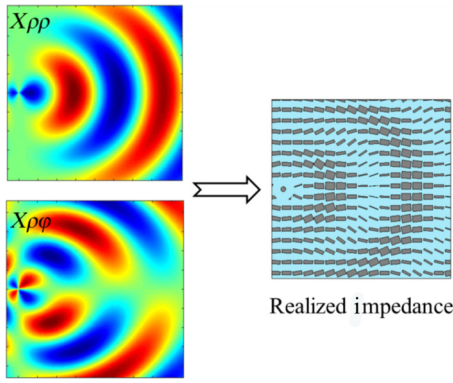
FIG. 18. Realization process of anisotropic impedance pattern using the proposed rectangular unit-cell.

of the rectangle (namely, b) and the rotation angle relative to the propagation direction (ψ). Rogers RO4003 with a thickness of 1.524 mm is chosen as the dielectric substrate. The tensorial impedance is calculated by the method proposed in Ref. [52]. The components of the impedance tensor can be written as follows:

$$X_{\rho\rho} = X_1 \cos^2 \psi + X_2 \sin^2 \psi, \tag{41}$$

$$X_{\phi\phi} = X_1 \sin^2 \psi + X_2 \cos^2 \psi, \tag{42}$$

$$X_{\rho\phi} = X_{\phi\rho} = (X_1 - X_2) \sin \psi \cos \psi, \tag{43}$$

where X_1 and X_2 are the relevant impedances aligned to the principle axes when $\psi = 0°$ (namely x and y, respectively). The process of calculating X_1 and X_2 is similar to the isotropic unit cell. Both parameters X_1 and X_2 are dependent on the geometrical parameters a and b. In this scenario, a is kept constant and b is taken as a variable. Figures 15(b) and 15(c) show the dispersion curves when the wave propagates in the x axis and y axis directions, respectively. In Figs. 16(a) and 16(b) the variations of $X_{\rho\rho}$ and $X_{\rho\phi}$ are illustrated as a function of the parameters b and ψ. Considering the calculations in the previous section, the values of $X_{\rho\rho}$ and $X_{\rho\phi}$ are clearly known at every point (x, y). Therefore, the value of b and ψ can be extracted at each point of the hologram using a least-squares method. For example, Figs. 17(a) and 17(b) show the required dimensions and rotation angles of the patches for the realization of surface impedance in Figs. 8(b) and 8(c). In order to clarify the accuracy of obtained parameters, the error in calculations is also measured, which is depicted in Fig. 17(c). Figure 18 show the surface impedance pattern and its corresponding synthesized hologram using rectangular patches. A conventional monopole is used for the hologram excitation. The length of the monopole is selected equal to a quarter wavelength. As the radiation from the monopole is omnidirectional and its main lobe is in the direction of $\theta = 90°$, it is expected that a large part of the power is directed on the surface. Metal via holes are used in order to realize
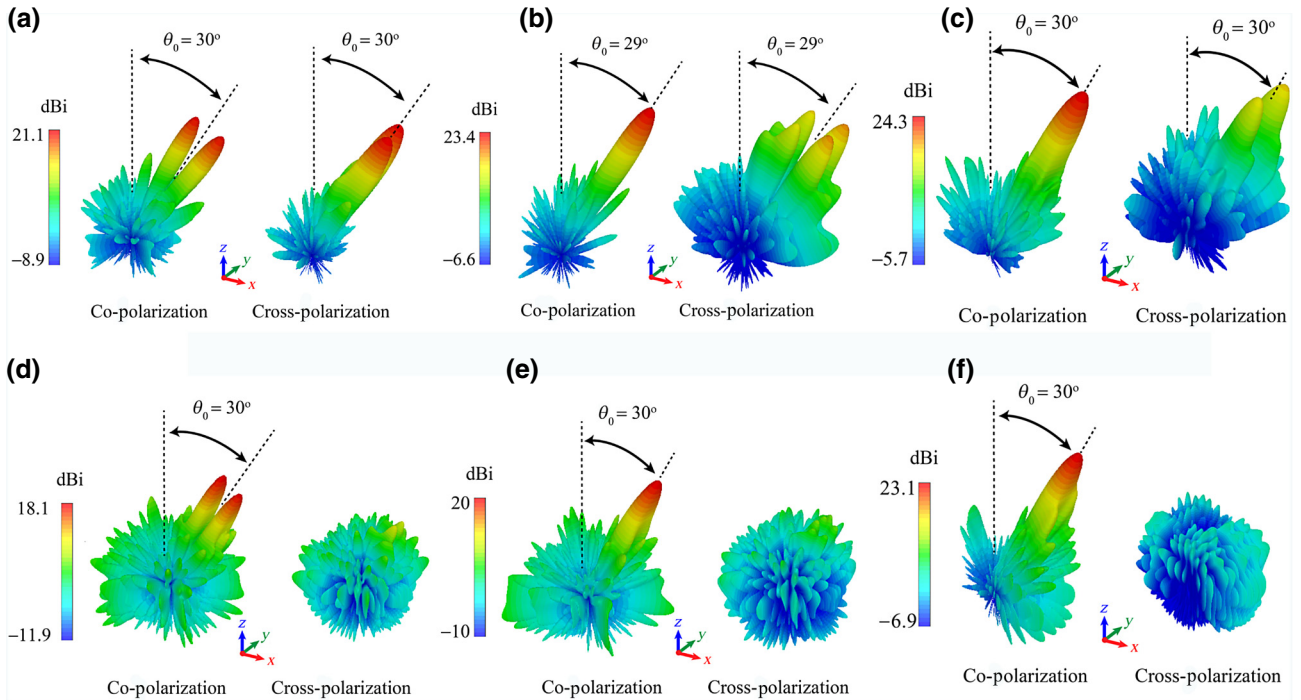

FIG. 19. 3D patterns of synthesized holograms in Sec. III: (a) conventional isotropic hologram; (b) phase-compensated isotropic hologram; (c) reflector-based isotropic hologram; (d) conventional anisotropic hologram; (e) phase-compensated anisotropic hologram; (f) reflector-based anisotropic hologram.
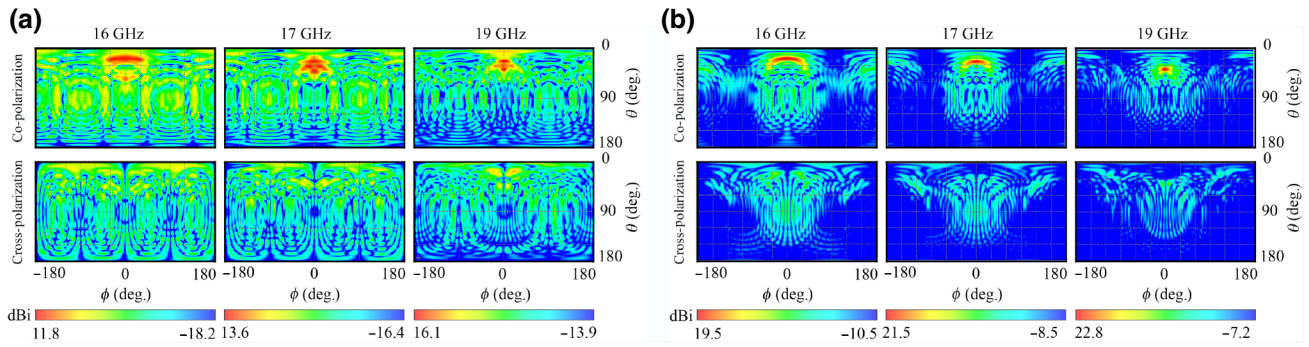
FIG. 20.   Comparison between the scannability of (a) phase-compensated anisotropic and (b) reflector-based anisotropic holograms.

the surface-wave reflector, which plays the role of a PEC boundary condition [53]. The radius of metal via holes and their spacings are chosen to minimize wave leakage.

V. SIMULATION RESULTS

A. Pencil beam hologram

The simulation results of different cases of conventional, phase-compensated, and reflector-based holograms are illustrated in Fig. 19. Simulations are performed in the transient solver of CST Studio [54]. The top row shows the results of isotropic structures and the bottom row is for the anisotropic cases. Note that the design parameters $(X_0, M, \theta_0, \text{ and } \phi_0)$ are selected equal for all the simulated examples, and the aperture area is considered $10\lambda \times 10\lambda$ for all the antennas. Figure 19(a) demonstrates the pattern of a conventional hologram with isotropic unit cells.

The cross-polarization component has the same level as its co-polarization. In addition, a null is observed exactly at the design angle (i.e., $\theta = 30°$), which is in accordance with the predicted results of Fig. 2. Figure 19(b) shows the pattern of a phase-compensated hologram. Observe that the cross-polarization component has four lobes with a level of 18.5 dB (i.e., 4.9 dB less than the main lobe), which is undesirable. Observe also in Fig. 19(c) that the co- and cross-polarization levels of the reflector-based antenna have improved compared with the conventional case. The results in Figs. 19(d)–19(f) show that the use of anisotropic surfaces in all three cases (conventional, phase-compensated, and reflector-based) significantly increases the co- to cross-polarization ratio. To compare the frequency scannability of the proposed antenna, in Fig. 20, far-zone patterns are depicted in two conditions: with and without a reflector. Observe that the
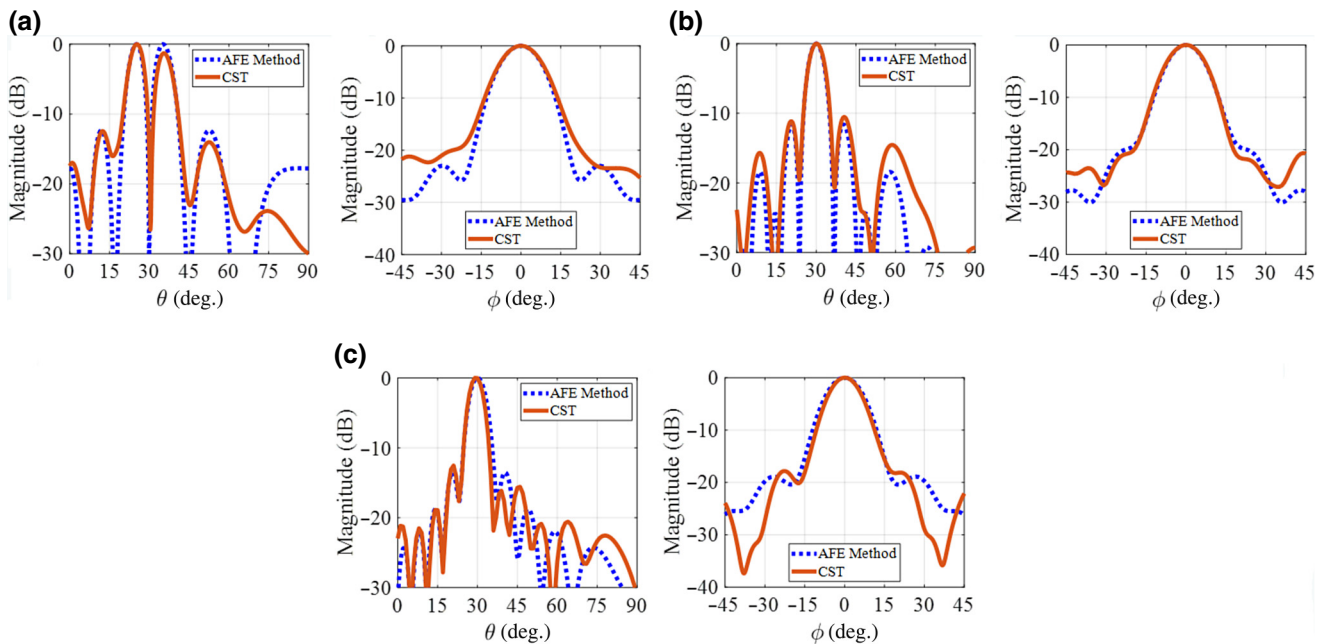

FIG. 21.   Comparison between the results of full-wave simulation and the AFE method for far-zone patterns of: (a) the conventional anisotropic hologram; (b) the phase-compensated anisotropic hologram; (c) the reflector-based anisotropic hologram.

TABLE I. Comparison between synthesized holograms in Sec. II.

Hologram type	Maximum co-polar directivity (dBi)	Maximum cross-polar directivity (dBi)	Side lobe level (dB)	Null	Scannability
Conventional isotropic hologram	20.6	21.1	−11.3	Yes	No
Phase-compensated isotropic hologram	23.4	18.5	−12.7	No	No
Reflector-based isotropic hologram	24.3	17.6	−13.4	No	Yes
Conventional anisotropic hologram	18.1	9.9	−9.2	Yes	No
Phase-compensated anisotropic hologram	20	7.9	−11.0	No	No
Reflector-based anisotropic hologram	23.1	5.5	−12.6	No	Yes

proposed antenna performance is in the range of 16–19 GHz, whereas the conventional antenna does not have the desired performance outside the frequency band. The gains of hologram without the reflector are 11.8, 13.6, and 16.1 dB for 16, 17, and 18 GHz, respectively. In contrast, for the reflector-based hologram, the obtained gains are 19.5, 21.6, and 22.8 dB, respectively. In addition, the cross-polarization component has an acceptable level in the frequency band. To evaluate the accuracy of the AFE method, the results of the analysis and full-wave simulation for anisotropic structures are compared. Figure 21 shows the E- and H-plane patterns of anisotropic holograms. Observe that the analytical method is sufficiently accurate to predict the far-zone pattern of leaky-wave holograms. In order to increase the accuracy of calculations, we can use the eigenmode method to estimate the surface-wave number. However, using this method increases the complexity of analysis and time of computations. Thus, there is a compromise between the accuracy of analysis and time of computations. Table I presents the quantitative comparison of simulated antennas. The reflector-based isotropic hologram has the largest directivity, which is a direct consequence of the reduction of diffraction caused by the surface-wave confinement.

The directivity of the reflector-based anisotropic hologram is approximately 1.4 dB lower than the isotropic one. The co- to cross-polarization ratio level, however, is improved significantly. In Table II, the performance of the proposed reflector-based hologram is compared. with other holograms in the literature. Despite the scan capability, the proposed hologram in Ref. [28] does not have a good cross-polarization level. The reported value for the cross-polarization level in Ref. [41] is −25 dB, which is appropriate. However, this antenna is operable at almost a single frequency. In Ref. [43], the maximum level of cross-polarization in the scan plane has been reported as approximately −20 dB. However, as mentioned in Sec. II, the cross-polarization of isotropic holograms at angles other than the design direction is undesirable.

B. Vortex-beam hologram

Figures 22(a) and 22(b) show the magnitude and phase profile of far-zone patterns for the hologram with a topological charge of $l = 2$. Its dimensions are selected as $14\lambda \times 14\lambda$. Observe that the magnitude of pattern shows a null at the broadside. For both F_θ and F_ϕ components, the maximum gain is 22.6 dB. In addition, in

TABLE II. Performance comparison of the proposed reflector-based anisotropic hologram with the other holograms.

| Ref.	Hologram type	Features	Bandwidth (GHz)	Polarization type	Maximum cross-polarization (scan plane)	Scannability
[21]	Isotropic	Multibeam	16–18	Vertical	...	Yes
[22]	Isotropic	Dual-functional	16.5–18	Vertical and horizontal	...	Yes
[28]	Anisotropic	Dual hand hologram	9.5–11	Circular	∼ − 6 dB at 10 GHz	Yes
[41]	Isotropic	Spiral modulated metasurface	17	Circular	∼ − 10 dB at 17 GHz	No
[41]	Anisotropic	Spiral modulated metasurface	8.425	Circular	∼ − 25 dB at 8.425 GHz	No
[43]	Isotropic	Phase-compensated hologram	19–21	Vertical and horizontal	∼ − 20 dB (vertical) and ∼ − 15 dB (horizontal) at 20 GHz	Yes
[47]	Anisotropic	Spiral modulated metasurface	20–30	...	...	No
This work	Anisotropic	Reflector-based hologram	16–19	Vertical	< − 30 dB in the bandwidth	Yes
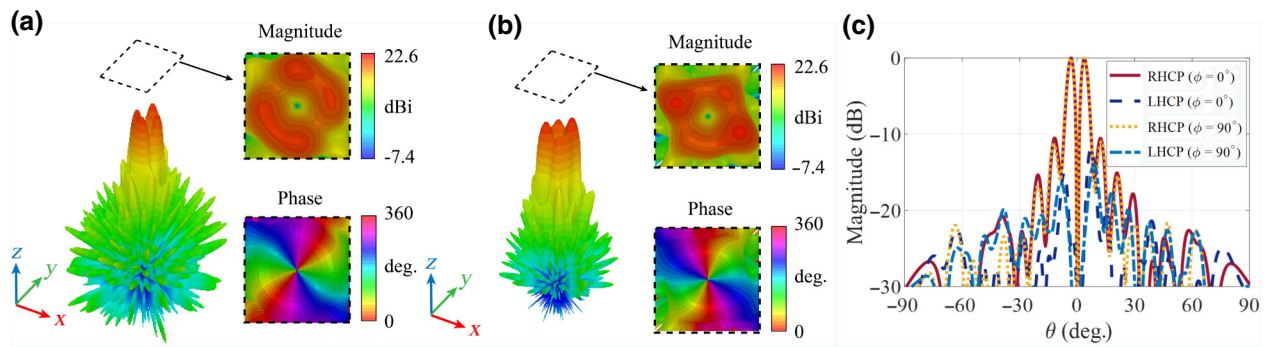
FIG. 22. Simulation results of the far-zone pattern at 18 GHz: (a) vertical component (F_θ); (b) horizontal component (F_ϕ); and (c) co- and cross-polarization components.

Fig. 22(c) the right-hand and left-hand components of the pattern are plotted. In this case, the cross-polarization (LHCP) is 14 dB lower than the co-polarization (RHCP) component.

VI. FABRICATION AND MEASUREMENT

As discussed in the previous section, the rectangular patches can be printed on the grounded dielectrics in order to realize the synthesized impedance surfaces. The dimensions of patches are different along x and y directions. Hence, the unit cells are anisotropic. The length and width of the unit cell are chosen, first to provide the proper resolution for the synthesis of impedance pattern, and second to determine the tensor of the required surface impedance. Figure 23 shows the fabricated structure of a hologram, consisting of two layers. The first is made of Rogers RO4003 with a standard thickness of 1.524 mm, on which the hologram is printed. The second layer is used for the implementation of a reflector. As the dielectric constant and dielectric losses do not affect the overall performance of the reflector, cost-efficient substrates can be used. In this case, we use FR-4 as the reflector substrate. Ideally, for the optimal reflection, the height of the reflector should be infinite, but owing to the fact that the wave is confined along the substrate in the vertical direction, a height of 3.2 mm (as the standard thickness of FR-4 substrate) is sufficient. In Fig. 23 the results of radiation pattern for both co- and cross-polarization components in the E and H planes are depicted. The simulation results are in good agreement with measurement data. It is observed that the maximum cross-components in the E and H planes are 33 dB and 20 dB less than the co-components, respectively.
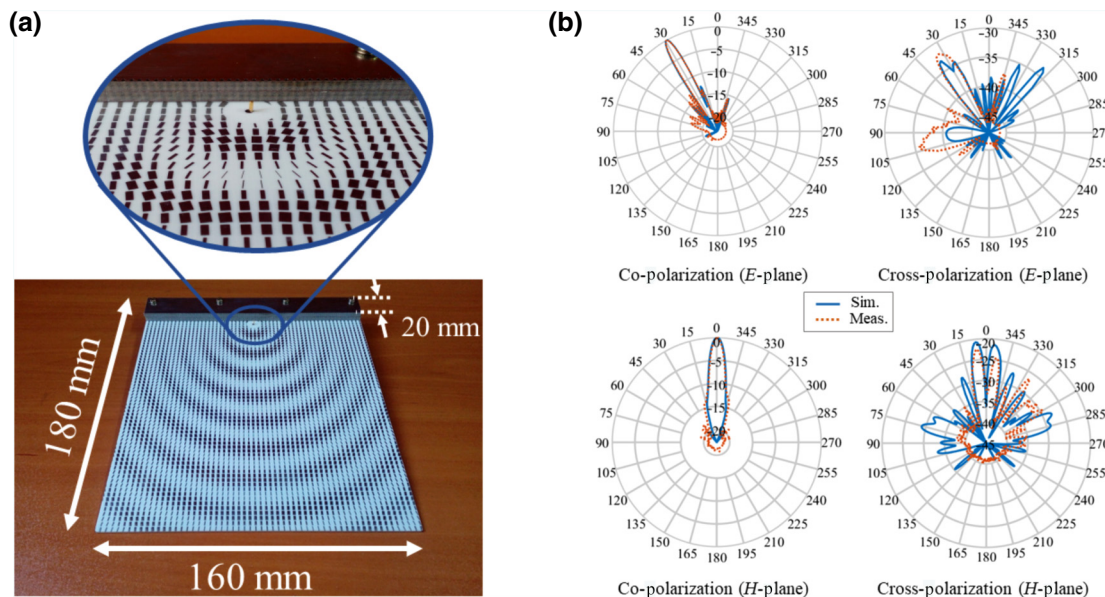

FIG. 23. (a) Fabricated prototype of the proposed reflector-based anisotropic hologram. (b) Simulation and measured patterns of the hologram at 18 GHz. All of the patterns are normalized to the maximum of co-polarization component.

VII. CONCLUSION

In this paper, a general method is proposed for the synthesis and design of (isotropic and anisotropic) holographic antennas. This method is based on the AFE theory to achieve the desired radiation beam and polarization. In this method, first the general orientation of beam and the desired polarization type are selected. Using the Fourier transformation, the aperture field is then approximated. Finally, the impedance pattern is synthesized by the generalized holography theory. The advantage of using AFE theory is its very high speed in estimating and analyzing the leaky-wave holographic antennas. For the given examples in this paper (of which the size is 10λ), the analysis time is a few minutes, whereas the simulation of an antenna by the full-wave simulator requires several hours. This method also gives the designer an overview of the synthesis of a hologram with the desired polarization, which is not possible with conventional holograms. In this paper, various structures of holograms are analyzed with the AFE theory. The aim is to find the most suitable choice for a linear polarization hologram. Studies show that the use of anisotropic structures significantly reduces the cross-polarization better than in previous works. The results of the full-wave simulations also confirm these results. Therefore, the AFE theory is well responsive to the design of leaky-wave holographic antennas. For further improvement of radiation characteristics, a surface-wave reflector is used to eliminate the destructive effect of backward mode on other frequencies. By eliminating the effect of backward mode, the frequency scanning feature is added to the hologram, which is suitable for the frequency modulated continuous wave (FMCW) radar systems. The achieved frequency bandwidth of the antenna performance is 17%.

[1] N. Yu, P. Genevet, M. A. Kats, F. Aieta, J. P. Tetienne, F. Capasso, and Z. Gaburro, Light propagation with phase discontinuities: Generalized laws of reflection and refraction, Science **334,** 333 (2011).

[2] N. Yu and F. Capasso, Flat optics with designer metasurfaces, Nat. Mater. **13,** 139 (2014).

[3] F. Monticone, N. M. Estakhri, and A. Alu, Full Control of Nanoscale Optical Transmission With a Composite Metascreen, Phys. Rev. Lett. **110,** 203903 (2013).

[4] C. Pfeiffer and A. Grbic, Metamaterial Huygens' Surfaces: Tailoring Wave Fronts with Reflectionless Sheets, Phys. Rev. Lett. **110,** 197401 (2013).

[5] M. R. M. Hashemi, S.-H. Yang, T. Wang, N. Sepúlveda, and M. Jarrahi, Electronically-controlled beam-steering through vanadium dioxide metasurfaces, Sci. Rep. **6,** 35439 (2016).

[6] Y. Chen, J. Gao, and X. Yang, Direction-controlled bifunctional metasurface polarizers, Laser Photon. Rev. **12,** 1800198 (2018).

[7] C. Pfeiffer and A. Grbic, Bianisotropic Metasurfaces for Optimal Polarization Control: Analysis and Synthesis, Phys. Rev. Appl. **2,** 044011 (2014).

[8] Z. Wu, Y. Ra'di, and A. Grbic, Tunable Metasurfaces: A Polarization Rotator Design, Phys. Rev. X **9,** 011036 (2019).

[9] M. Khorasaninejad, W. T. Chen, R. C. Devlin, J. Oh, A. Y. Zhu, and F. Capasso, Metalenses at visible wavelengths: Diffraction-limited focusing and subwavelength resolution imaging, Science **352,** 1190 (2016).

[10] H. Yang, X. Cao, F. Yang, J. Gao, S. Xu, M. Li, X. Chen, Y. Zhao, Y. Zheng, and S. Li, A programmable metasurface with dynamic polarization, scattering and focusing control, Sci. Rep. **6,** 35692 (2016).

[11] S. R. Biswas, C. E. Gutiérrez, A. Nemilentsau, I. Lee, S. Oh, P. Avouris, and T. Low, Tunable Graphene Metasurface Reflectarray for Cloaking, Illusion, and Focusing, Phys. Rev. Appl. **9,** 034021 (2018).

[12] D. J. Gregoire and A. V. Kabakian, Surface-wave waveguides, IEEE Antennas Wirel. Propag. Lett. **10,** 1512 (2011).

[13] R. G. Quarfoth and D. F. Sievenpiper, Nonscattering waveguides based on tensor impedance surfaces, IEEE Trans. Antennas Propag. **63,** 1746 (2015).

[14] D. J. Bisharat and D. F. Sievenpiper, Guiding Waves Along an Infinitesimal Line between Impedance Surfaces, Phys. Rev. Lett. **119,** 106802 (2017).

[15] Z. Xu, X. Yin, and D. F. Sievenpiper, Adiabatic Mode-Matching Techniques for Coupling between Conventional Microwave Transmission Lines and One Dimensional Impedance-Interface Waveguides, Phys. Rev. Appl. **11,** 044071 (2019).

[16] H. Liu and K. J. Webb, Leaky wave radiation from planar anisotropic metamaterial slabs, Phys. Rev. B **81,** 201404(R) (2010).

[17] F. Monticone and A. Alu, Leaky-wave theory, techniques, and applications: From microwaves to visible frequencies, Proc. IEEE **103,** 793 (2015).

[18] S. N. Tcvetkova, D.-H. Kwon, A. Díaz-Rubio, and S. A. Tretyakov, Near-perfect conversion of a propagating plane wave into a surface wave using metasurfaces, Phys. Rev. B **97,** 115447 (2018).

[19] M. Memarian and G. V. Eleftheriades, Dirac leaky-wave antennas for continuous beam scanning from photonic crystals, Nat. Commun. **6,** 5855 (2015).

[20] P. Checcacci, V. Russo, and A. Scheggi, Holographic antennas, IEEE Trans. Antennas Propag. **18,** 811 (1970).

[21] Y. B. Li, X. Wan, B. G. Cai, Q. Cheng, and T. J. Cui, Frequency-controls of electromagnetic multi-beam scanning by metasurfaces, Sci. Rep. **4,** 6921 (2014).

[22] Y. B. Li, B. G. Cai, Q. Cheng, and T. J. Cui, Isotropic holographic metasurfaces for dual-functional radiations without mutual interferences, Adv. Funct. Mater. **26,** 29 (2015).

[23] Y. B. Li, A. Li, T. J. Cui, and D. F. Sievenpiper, Multiwavelength multiplexing hologram designed using impedance metasurfaces, IEEE Trans. Antennas Propag. **66,** 6408 (2018).

[24] Z. Khitab, F. A. Bhatti, A. A. Khan, A. M. Siddiqui, and I. Rashid, in *2017 IEEE 6th Global Conference on Consumer Electronics (GCCE)* (IEEE, Nagoya, Japan, 2017), p. 1.

[25] A. Ludwig, The definition of cross polarization, IEEE Trans. Antennas Propag. **21,** 116 (1973).

[26] S. Pandi, C. A. Balanis, and C. R. Birtcher, Design of scalar impedance holographic metasurfaces for antenna beam formation with desired polarization, IEEE Trans. Antennas Propag. **63,** 3016 (2015).

[27] B. H. Fong, J. S. Colburn, J. J. Ottusch, J. L. Visher, and D. F. Sievenpiper, Scalar and tensor holographic artificial impedance surfaces, IEEE Trans. Antennas Propag. **58,** 3212 (2010).

[28] X. Wan, T. Y. Chen, Q. Zhang, J. Y. Yin, Z. Tao, L. Zhang, X. Q. Chen, Y. B. Li, and T. J. Cui, Manipulations of dual beams with dual polarizations by full-tensor metasurfaces, Adv. Opt. Mater. **4,** 1567 (2016).

[29] X. Meng, J. Wu, Z. Wu, L. Yang, L. Huang, X. Li, T. Qu, and Z. Wu, Generation of multiple beams carrying different orbital angular momentum modes based on anisotropic holographic metasurfaces in the radio-frequency domain, Appl. Phys. Lett. **114,** 093504 (2019).

[30] D. Gonzlez-Ovejero and S. Maci, Gaussian ring basis functions for the analysis of modulated metasurface antennas, IEEE Trans. Antennas Propag. **63,** 3982 (2015).

[31] M. Bodehou, D. Gonzlez-Ovejero, C. Craeye, and I. Huynen, Method of moments simulation of modulated metasurface antennas with a set of orthogonal entire-domain basis functions, IEEE Trans. Antennas Propag. **67,** 1119 (2019).

[32] M. Teniou, H. Roussel, N. Capet, G. Piau, and M. Casaletti, Implementation of radiating aperture field distribution using tensorial metasurfaces, IEEE Trans. Antennas Propag. **65,** 5895 (2017).

[33] C. A. Balanis, *Antenna Theory: Analysis and Design* (John Wiley & Sons, New York, 2016), 4th ed.

[34] J. W. Goodman, *Introduction to Fourier Optics* (Roberts and Company Publishers, Englewood, Colorado, 2005), 3rd ed.

[35] X. Gao, S. Huang, Y. Wei, W. Zhai, W. Xu, S. Yin, J. Zhou, and W. Gu, An orbital angular momentum radio communication system optimized by intensity controlled masks effectively: Theoretical design and experimental verification, Appl. Phys. Lett. **105,** 241109 (2014).

[36] M. Karimipour, N. Komjani, and I. Aryanian, Holographic-Inspired Multiple Circularly Polarized Vortex-Beam Generation with Flexible Topological Charges and Beam Directions, Phys. Rev. Appl. **11,** 054027 (2019).

[37] Z. Wang, S. Dong, W. Luo, M. Jia, Z. Liang, Q. He, S. Sun, and L. Zhou, High-efficiency generation of Bessel beams with transmissive metasurfaces, Appl. Phys. Lett. **112,** 191901 (2018).

[38] Z. Zhang, S. Zheng, X. Jin, H. Chi, and X. Zhang, Generation of plane spiral oam waves using traveling-wave

[39] circular slot antenna, IEEE Antennas Wirel. Propag. Lett. **16,** 8 (2017).

[39] D. Gabor, A new microscopic principle, Nature **161,** 777 (1948).

[40] H. Oraizi, A. Amini, A. Abdolali, and A. M. Karimimehr, Design of wideband leaky-wave antenna using sinusoidally modulated impedance surface based on the holography theory, IEEE Antennas Wirel. Propag. Lett. **17,** 1807 (2018).

[41] G. Minatti, M. Faenzi, E. Martini, F. Caminita, P. De Vita, D. Gonzlez-Ovejero, M. Sabbadini, and S. Maci, Modulated metasurface antennas for space: Synthesis, analysis and realizations, IEEE Trans. Antennas Propag. **63,** 1288 (2015).

[42] D. J. Hoppe and Y. Rahmat-Samii, *Impedance Boundary Condition in Electromagnetics* (Taylor and Francis, Washington, DC, 1995), 1st ed.

[43] M. Casaletti, M. Smierzchalski, M. Ettorre, R. Sauleau, and N. Capet, Polarized beams using scalar metasurfaces, IEEE Trans. Antennas Propag. **64,** 3391 (2016).

[44] M. M. Moeini, H. Oraizi, and A. Amini, Collimating Cylindrical Surface Leaky Waves for Highly Improved Radiation Characteristics of Holograms, Phys. Rev. Appl. **11,** 044006 (2019).

[45] M. M. Moeini, H. Oraizi, and A. Amini, in *2018 48th European Microwave Conference (EuMC)* (IEEE, Madrid, 2018), p. 428.

[46] COMSOL Multiphysics, https://www.comsol.com/.

[47] M. Faenzi, G. Minatti, D. Gonzlez-Ovejero, F. Caminita, E. Martini, C. Della Giovampaola, and S. Maci, Metasurface antennas: New models, applications and realizations, Sci. Rep. **9,** 10178 (2019).

[48] L. Allen, M. W. Beijersbergen, R. J. C. Spreeuw, and J. P. Woerdman, Orbital angular momentum of light and the transformation of Laguerre-Gaussian laser modes, Phys. Rev. A **45,** 8185 (1992).

[49] P. Vaity and L. Rusch, Perfect vortex beam: Fourier transformation of a bessel beam, Opt. Lett. **40,** 597 (2015).

[50] R. E. Collin and F. J. Zucker, *Antenna Theory* (McGraw-Hill, New York, 1969).

[51] M. Bosiljevac, M. Casaletti, F. Caminita, Z. Sipus, and S. Maci, Non-uniform metasurface luneburg lens antenna design, IEEE Trans. Antennas Propag. **60,** 4065 (2012).

[52] D. H. Werner and D. H. Kwon, *Transformation Electromagnetics and Metamaterials: Fundamental Principles and Applications* (Springer-Verlag, London, 2014).

[53] F. Xu and K. Wu, Guided-wave and leakage characteristics of substrate integrated waveguide, IEEE Trans. Antennas Propag. **53,** 66 (2005).

[54] CST Studio Suite, Computer Simulation Technolog ag, https://www.cst.com/.